Research Article Vol. 4, No. 7 / July 2017 / Optica 770

optica

Universal weighted synthetic aperture focusing technique (W-SAFT) for scanning optoacoustic microscopy

Jake Turner,[1,2] Héctor Estrada,[1] Moritz Kneipp,[1,3] and Daniel Razansky[1,3,*]

[1]Institute of Biological and Medical Imaging (IBMI), Helmholtz Center Munich, Ingolstädter Landstraße 1, 85764 Neuherberg, Germany
[2]Faculty of Electrical Engineering and Information Technology, Technische Universität München, Theresienstraße 90, 80333 Munich, Germany
[3]Faculty of Medicine, Technische Universität München, Ismaninger Straße 22, 81675 Munich, Germany
*Corresponding author: dr@tum.com

Received 1 August 2016; revised 17 May 2017; accepted 20 May 2017 (Doc. ID 272648); published 6 July 2017

Optoacoustic microscopy (OAM) is a hybrid imaging method that can achieve high spatial resolution at superficial depths through use of focused illumination; it can be adapted for imaging with ultrasonic resolution at much greater depths where the excitation light is diffuse. These two distinct modes of operation can be further combined to create a highly scalable technique that can image at multiple penetration scales by gradually exchanging microscopic optical resolution in superficial tissue layers with ultrasonic resolution at diffuse (macroscopic) depths. However, OAM commonly employs scanning acquisition geometries that impede the effective use of synthetic aperture focusing techniques due to varying illumination patterns and non-uniformity of the excitation light field. Here we present a universal framework for scanning optoacoustic microscopy that uses a weighted synthetic aperture focusing technique (W-SAFT) to create a uniform imaging sensitivity across microscopic, mesoscopic, and macroscopic penetration regimes. Robust performance of the new multi-scale reconstruction methodology is showcased with simulations and synthetic phantoms, and validated with experimental data acquired from a highly scattering juvenile zebrafish specimen. It is shown that consideration of the light fluence is vital for maintaining the optically dictated lateral resolution at ballistic depths while optimizing the resolution of out-of-focus ultrasonic data; additionally, the dynamic-range compression facilitates the visualization across the entire imaged volume. The newly introduced W-SAFT reconstruction framework is universally applicable to a wide palette of scanning-based optoacoustic imaging techniques employing non-uniform and/or varying illumination, such as acoustic resolution and hybrid focus microscopy, raster-scan optoacoustic mesoscopy, as well as tomographic approaches using scanning of focused array transducers.

OCIS codes: (110.3010) Image reconstruction techniques; (110.0180) Microscopy; (110.5125) Photoacoustics.

https://doi.org/10.1364/OPTICA.4.000770

1. INTRODUCTION

In optoacoustic imaging, broadband ultrasound waves are generated by laser-induced thermoelastic expansion. Due to the low acoustic scattering of soft biological tissues, optoacoustics is able to render images with diffraction-limited ultrasonic spatial resolution at millimeter to centimeter penetration scales non-invasively [1,2]. This capability makes optoacoustics a promising modality for applications in biomedical imaging and microscopy.

Scanning optoacoustic microscopy (OAM) comes in two main variants. In acoustic resolution (AR) [3] microscopy, a focused ultrasound transducer is used while the excitation is usually significantly broader than the field of view (FOV) of the transducer [Fig. 1(a)], whereas in optical resolution (OR) microscopy [4–6] an unfocused ultrasound transducer is commonly employed, with the lateral resolution dictated by the beam width of the focused illumination at a given depth [Fig. 1(b)]. The AR approach can image many millimeters to centimeters deep in optically scattering media [3], though the achievable resolution is established by the numerical aperture, bandwidth, and sensitivity of the transducer as well as the frequency-dependent ultrasound attenuation of the imaged tissues [7]. Furthermore, the lateral resolution outside the focal area of the transducer can be restored through methods such as the virtual detector method [8], synthetic aperture focusing technique (SAFT) [9], and model matrix inversion [10,11].

On the other hand, when considering an optically non-scattering medium with an illumination beam of low divergence, the achievable lateral resolution of the OR method can theoretically approach the optical diffraction limit. However, biomedical imaging typically targets optically opaque tissues, limiting the effective penetration of the modality to about a millimeter in highly scattering tissues [1]. Overall, OR microscopy is capable

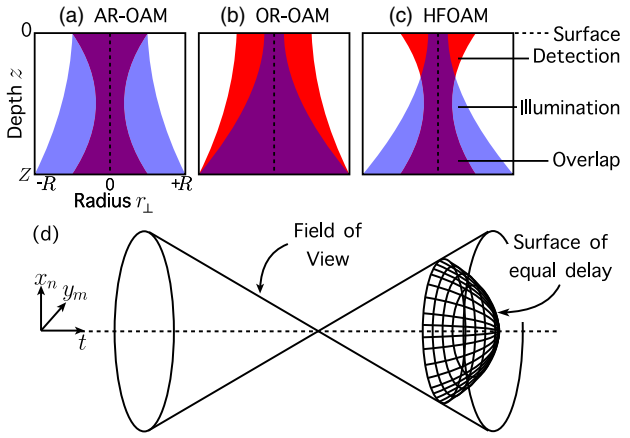

Fig. 1. Illustrations of the extent of the axially symmetric fields of light fluence (blue) and ultrasound-transducer field of view (red) as functions of depth z and polar-radius (radius to the focal axis) $r_\perp$. (a) Acoustic resolution (AR) case with broad illumination and focused detection, (b) optical resolution (OR) case with a focused illumination, (c) hybrid resolution optoacoustic microscopy (HFOAM) using both focused illumination and detection, (d) illustration of the 3D-SAFT operation.

of achieving greater resolution than AR microscopy, though the latter is the only applicable approach for deep-tissue imaging.

More recently, hybrid focus optoacoustic microscopy (HFOAM) systems, which employ a combination of focused illumination and ultrasound detection, have been developed [12,13]. These scalable approaches are aimed at gradually exchanging optical resolution in the superficial regime for an acoustic resolution at depths where the light is diffuse. However, efficient image reconstruction is impeded by lack of algorithms capable of restoring the out-of-focus lateral resolution in the AR regime while not impairing the lateral resolution in the OR regime. Additionally, although computationally fast, SAFT or other existing delay-and-sum–based image-reconstruction algorithms do not address the issue of a moving and heterogeneous light fluence distribution, as they are based on the assumption of a pure AR imaging scenario and thus homogeneous illumination.

Here we present a universal weighted synthetic aperture focusing technique (W-SAFT) to account for arbitrary scanning fluence in OAM systems. Our framework, conceived as a distortion-correction approach, aims to be applied in three dimensions through the full scan volume, including the acoustic focus, and to any variant of OAM using scanning ultrasound transducers and non-uniform or moving illumination. By considering the transducer sensitivity, optical beam properties, and optical properties of the imaged target, the algorithm aims to compensate for any distortions that SAFT introduces into the OAM data. Additionally, the dynamic range of peak–peak signal amplitudes is compressed to improve data visualization while preserving the relative strength of the different optical absorbers in the corrected images.

2. THEORY

A. Background

Most scanning OAM systems translate the ultrasound transducer and illumination source simultaneously in order to acquire time-domain optoacoustic waveforms from a set of scanned points in the lateral x–y plane. Typically, two linearly spaced arrays of $\{x_1, \ldots, x_N\}$ and $\{y_1, \ldots, y_M\}$ define a regular grid of measurement locations in the lateral plane. The scan volume $\boldsymbol{D}$ of such systems therefore consists of (N, M, J) voxels that are spatially defined at (x, y, z) coordinates, where $z = c_0 j/f_s$, c_0 is the speed of sound, f_s is the temporal sampling frequency, and J is the number of sampled time instants ($j = \{1, \ldots, J\}$). The instantaneous center of the volume is given as $(x', y', z') = (x_n - x_k, y_m - y_l, z - z_f)$, where $k = 1, \ldots, N$, $l = 1, \ldots, M$, and z_f is the focal length of the transducer. This distinction is necessary as, although the (x, y, z) space is intuitive in viewing the data volumes, the W-SAFT algorithm works in the (x', y', z') space.

The optoacoustic signals are only detected from locations where optical absorbers are both located within the FOV of the ultrasound transducer and illuminated by the short-duration laser light. As can be seen in Fig. 1(a), for AR microscopy the entire transducer's FOV falls within the limits of the diffuse light fluence, and thus any optical absorber within the FOV will yield a measured signal. Conversely, in the OR regime [Fig. 1(b)], the same FOV is only partially illuminated and thus not all the optical absorbers within the transducer's FOV inherently generate an acoustic wave to detect. At shallow depths, before the incident illumination is divergent, HFOAM essentially produces OR-type data, whereas at greater depth the illumination is equal to or broader than the extent of the FOV of the transducer, producing AR data [Fig. 1(c)].

In the case of scanning a geometrically focused ultrasound transducer, SAFT would use a delay-and-sum–based operation to restore the lateral resolution away from the acoustic focus [8,9]. Thus, the reconstructed FOV for each lateral transducer position will overlap with the adjacent reconstructed FOVs. By summing these regions along 3D surfaces of equal delay to the focus, SAFT improves the lateral resolution in the entire imaged volume, as illustrated in Fig. 1(d). Following [9], the discretized 3D SAFT operation can be written as

$$\sigma_{nm}(t) = \Gamma_{nmkl}(t) D_{kl}(t - \Delta t), \tag{1}$$

where $\sigma_{nm}(t)$ is the SAFT result at (x_n, y_m), Γ_{nmkl} is a binary weighting mask (1 inside the FOV, 0 elsewhere) that dictates the contributions of the summation, and $D_{kl}(t - \Delta t)$ is the delayed time-domain signal. The routine of applying the SAFT operation [Eq. (1)] at each transducer position can be written as

$$\mathbf{V} = \mathtt{SAFT}(D, \boldsymbol{\Gamma}), \tag{2}$$

where $\mathbf{V}$ is the output volume containing the SAFT-processed data.

This operation is readily applied to AR data; however, for OR microscopy or the OR-to-AR transitional (mesoscopic) regime in HFOAM, the pure SAFT approach will blur data in all x–y planes where the fluence width is narrower than the lateral acoustic beam size of the focused transducer. One further artifact in the results of SAFT-processed optoacoustic data is an amplitude bias for out-of-focus sources. This distortion occurs because, unlike scatterers in pulse-echo ultrasonics, optoacoustic signals are produced in all locations reached by the excitation light, independently from the acoustic focusing characteristics of the transducer. Therefore, out-of-focus sources may contribute very significantly to the SAFT summation [9]. This is herein referred to as the refocusing distortion.

B. W-SAFT Algorithm

W-SAFT makes use of weights to (a) limit the projection of voxels according to the illumination (including the sample's geometry) and the transducer's FOV, and (b) compensate for the refocusing and fluence distortions.

Any consideration of the light fluence must take into account the shape of the sample's surface $S(x, y)$, which can be discretized and grouped in I subsets according to their depth S_i with $i = 1:I$ (Fig. 2, first row). A model of the light fluence is then split to separately account for the fluence extent in the lateral dimension $\boldsymbol{U}_i$ and to compensate for the decay along the depth $\boldsymbol{G}_i$. In order to keep the fluence extent consistent with the physical mechanism of generation and detection of the pressure waves, $\boldsymbol{U}_i$ is normalized relative to the spherical surface along which the SAFT summation is being performed. Normalization in other coordinate systems would destroy the relative amplitudes between sources located at the same distance of the detector's focus. On the other hand, $\boldsymbol{G}_i$ is only a function of z and, for simplicity, we approximated it as an exponential gain $\boldsymbol{G}_i = e^{\alpha z}$, where $\alpha \geq 0$.

The characteristics of the ultrasound detector are included as the maximum amplitude projection (MAP) in time of the 4D spatial impulse response (SIR) $\boldsymbol{H}$.

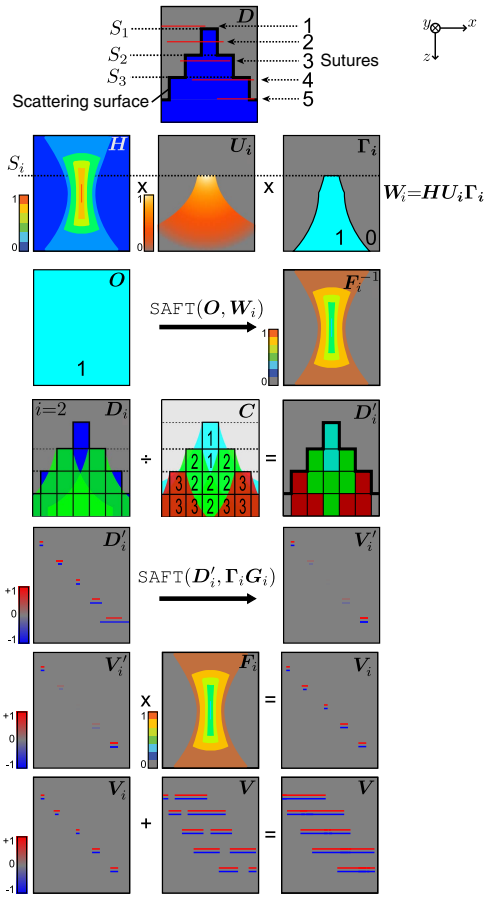

Fig. 2. Schematic illustration of the process of implementing W-SAFT. The top row is a diagram of the illustrative imaging target containing five sutures, each of which are within the scattering and non-scattering portions of the phantom to a varying degree. Each subsequent row of the figure corresponds to one line in Eq. (8); in row 4, color indicates depth iteration.

The binary mask $\boldsymbol{\Gamma}_i$ is then defined by the element-wise product between $\boldsymbol{H}$ and $\boldsymbol{U}_i$ as

$$\boldsymbol{\Gamma}_i = \begin{cases} 1, & \text{if } \boldsymbol{H}\boldsymbol{U}_i > k \\ 0, & \text{otherwise,} \end{cases} \tag{3}$$

where k is a threshold value. Now one may define a weighting-masking function (Fig. 2, row 2)

$$\boldsymbol{W}_i = \boldsymbol{H}\boldsymbol{U}_i\boldsymbol{\Gamma}_i \tag{4}$$

to generate the normalization factor that compensates for the refocusing distortion

$$\boldsymbol{F}_i = 1/\mathrm{SAFT}(\boldsymbol{O}, \boldsymbol{W}_i), \tag{5}$$

where $\boldsymbol{O} = 1\ \forall(x, y, z)$ (Fig. 2, row 3). As a result of using $\boldsymbol{\Gamma}_i$, the data is separated in subsets $\boldsymbol{D}_i$ and voxels contribute differently to the total volume during application of the SAFT operation (see Fig. 2, row 4). If ignored, this cumulative effect leads to a large signal amplitude bias, particularly strong in the AR regime due to the larger width of the $\boldsymbol{\Gamma}_i$ masks. A count-matrix, $\boldsymbol{C}$, is calculated to compensate for this distortion as

$$\boldsymbol{C} = \sum_i^n \boldsymbol{\Gamma}_i, \tag{6}$$

to define $\boldsymbol{D}'_i = \boldsymbol{D}_i/\boldsymbol{C}$. Eventually, $\boldsymbol{D}'_i$ is projected and corrected for fluence decay (Fig. 2, row 5)

$$\boldsymbol{V}'_i = \mathrm{SAFT}(\boldsymbol{D}'_i, \boldsymbol{\Gamma}_i\boldsymbol{G}_i), \tag{7}$$

and the result is compensated for the refocusing distortion $\boldsymbol{V}_i = \boldsymbol{V}'_i\boldsymbol{F}_i$ (Fig. 2, row 6). Iterating the procedure for all the different surface levels yields

$$\begin{aligned} &\text{for } i = 1:I\{ \\ &\quad \boldsymbol{W}_i = \boldsymbol{H}\boldsymbol{U}_i\boldsymbol{\Gamma}_i \\ &\quad \boldsymbol{F}_i = 1/\mathrm{SAFT}(\boldsymbol{O}, \boldsymbol{W}_i) \\ &\quad \boldsymbol{D}'_i = \boldsymbol{D}_i/\boldsymbol{C} \\ &\quad \boldsymbol{V}'_i = \mathrm{SAFT}(\boldsymbol{D}'_i, \boldsymbol{\Gamma}_i\boldsymbol{G}_i) \\ &\quad \boldsymbol{V}_i = \boldsymbol{V}'_i\boldsymbol{F}_i \\ &\} \\ &\boldsymbol{V} = \sum_i^I \boldsymbol{V}_i, \end{aligned} \tag{8}$$

which is depicted in Fig. 2. As the excitation fluence distribution does not remain constant in the lateral plane, it is imperative that correction $\boldsymbol{G}_i$ be included in the SAFT operation [Eq. (7)] and not as a pre- or post-correction step. Note that our approach does not dictate the most appropriate method for fluence estimation, which is a complex research topic unto itself. For the current investigation, models of embedded Gaussian beams [14] were used, where the un-scattered incident beam $v(x', y', z)$ was defined by beam waist values chosen from the geometrical properties of the illumination optics [15]. With this model, the beam waist at the optically scattering surface $S(x, y)$ could then be determined. Taking the at-surface beam waist of the unscattered beam, an at-depth scattered beam waist was selected. With these two beam waists, the M^2 value for the scattered beam was calculated, as was the beam waist at all depths inside the scattering volume, giving the scattered beam $\boldsymbol{U}_i$. To model the scattered beam for experimental data, an estimate of the beam spread at a certain depth

inside the imaging target needed to be made. This was achieved by manually selecting a structure inside the imaging target and iteratively running many instances of W-SAFT while varying the at-depth beam waist. The metric against which different waists were rated were the FWHM of the selected structure and the FWHM of any deeper structures. The minimal criterion was that the FWHM of the selected structure should not be degraded; the maximum criterion was that the FWHM of both the selected structure and deeper structures should be improved.

Although any simulated attenuation can readily be used to modulate $\boldsymbol{U}_i$, in the experimental case the attenuation must be estimated. For the experimental data presented in the following sections, the fluence attenuation was estimated based on fitting curves to the instances of $\boldsymbol{V}_i$ as returned by Eq. (8) without $\boldsymbol{G}_i$. This was deemed appropriate, as fluence attenuation is the major cause of decreasing signal amplitude along the z direction. Because of the surface-depth-dependent nature of $\boldsymbol{V}_i$, the gain function is also estimated on a per-surface-depth basis.

One major limitation in the peak-to-peak amplitude equalization of signals from sources in the optically dictated resolution regime is, intuitively, that as not all possible lateral contributions exist, the superposition necessary for full peak–peak equalization cannot be achieved. Therefore, the peak-to-peak amplitude equalization is best considered as a dynamic range compression. Additionally, this limited-contribution scenario will limit the potential for improving spatial resolution.

3. METHODS

In the development and assessment of the new algorithm, four data sets were used. The first was the previously simulated data set, the second and the third were experimental scans of a suture phantom in clear or scattering agar, and the fourth was an *ex vivo* scan of a scattering juvenile zebrafish sample.

The simulated and experimental scans covered different areas and thus used different scanning resolutions; the voxel size therefore varies between the data sets. This variation was necessary owing to limitations in the microscopy system with respect to scan size, scan mode, scan resolution, and signal averaging.

In the post-processing of the simulated and experimental scans, a PC with 64 GB RAM, 3.2 GHz processor (i7 3930, Intel, USA), and a GPU with 2304 cores and 3 GB onboard memory (GeForce GTX 780, Nvidia, USA) was used.

A. Simulated Scan

For initial performance testing, a scan was simulated along a synthetic phantom containing nine microspheres of 60 μm diameter. The microspheres were arranged at equal vertical intervals between ±1.4 mm from the acoustic focus and spaced uniformly in a 3 × 3 grid in both lateral directions between ±1 mm from the center of the imaged volume. The scattering optical surface was modeled as a discretized dome of concentric rings having uniform depth and equal step size [see Fig. 3(a)]. The modeled Gaussian-beam fluence was also subject to an additional

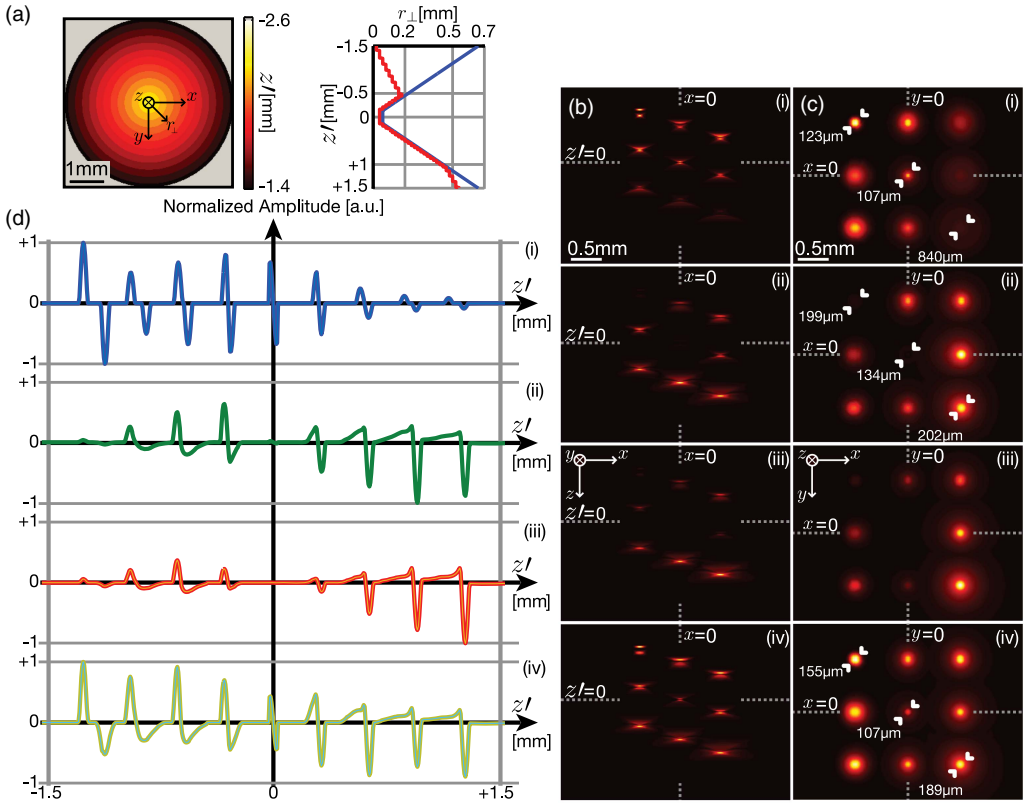

Fig. 3. (a) Left: depth profile of the optically scattering surface $S(x, y)$, where gray is no-surface; right: $\boldsymbol{\Gamma}$ (red) and $\boldsymbol{H}$ (blue) evaluated at z'. (b) MAPs through y and (c) MAPs through z. (i) simulated data, $\boldsymbol{D}$; (ii) results of weighted SIR-SAFT; (iii) intermediate result of W-SAFT using only limit function $\boldsymbol{\Gamma}$ [Eq. (3)]; (iv) complete result of W-SAFT with all distortion corrections, $\boldsymbol{V}$ [Eq. (8)]. (c) also shows annotations of FWHM for three of the spheres. (d) shows the composite time-domain center shots for (i–iv), i.e., superpositions of the time-domain signals for the center of each sphere.

attenuation-modeling gain of −12 dB/cm below the scattering surface. The simulated 3D image grid consisted of voxels with 20, 20, and 6 μm in the x, y, and z directions, respectively.

The optoacoustic signals generated by the microspheres were calculated as per [16], and to model the detection of the pressure signals by the transducer, the Field-II software was used [17]. The modeled transducer was that of the previously reported HFOAM system [12], i.e., a water-coupled spherically focused PVDF transducer (Precision Acoustics, UK) with a center frequency of 30 MHz, >100% bandwidth, focal distance of 7.1 mm, and an active diameter of 6 mm, resulting in a focal spot with −6 dB size $(r_\perp, z) = (80, 620)$ μm. The transducer also has a 0.9 mm hole through its center, through which an optical fiber assembly can be inserted. The system is also capable of using the same transducer to acquire concurrent pulse-echo ultrasound images [18].

The transducer was simulated as broadband, and subsequently the final data set could be filtered to simulate the effects of any electrical impulse response; Field-II was also used to simulate the SIR of the transducer. To reduce runtime in computing the simulated scan, the axial symmetry of the microspheres, transducer, and incident fluence was exploited. Namely, the pressure signals detected for each sphere $p(t)$ were modeled not for all pairs of (x, y) but rather for all unique values of the radii r, i.e., $(r) = \sqrt{x_n^2 + y_m^2}$. Subsequently, the simulated data was extruded about the instantaneous z axis (the sphere center) at (x', y', z). This sub-volume $\boldsymbol{D}_i$ could then be weighted by the subset of the moving fluence incident over the sphere, which is dependent on the corresponding subset of the surface $\boldsymbol{S}_i$, and summed into the master volume $\boldsymbol{D}$.

B. Phantom Scan

Two phantoms were made with sutures of 50 μm cross-sectional diameter mounted in a cylinder of agar. In phantom A, the agar was non-scattering and contained six sutures, whereas phantom B was highly scattering (1% v/v intralipid concentration) and contained five sutures. The purpose of these phantoms was to demonstrate the application of the proposed algorithm to experimental data in both the OR and AR regimes.

The scans were performed with a fast-scanning HFOAM system that uses the aforementioned spherically focused PVDF ultrasound transducer for detection [12], operating in raster-scan mode so that signal averaging could be used to ensure high SNR. Illumination was delivered through a multimode fiber with an NA of 0.39 and core diameter of 600 μm (FT600UMT, Thorlabs, DE). The scan performed on phantom A covered a region of 3 × 3 mm in the lateral plane in square steps of 30 μm, with a pulse-repetition frequency of 1 kHz and a per-pulse energy of around 275 μJ; the scans were made with 50 averages per position. The scan of phantom B was over a larger region of 9 × 9 mm with steps of 60 μm and 350 averages per position. High optical energy and significant averaging were used here to ensure the deepest of the sutures could be well detected. These structures were significantly deep for the acoustic focus, and therefore the scan data would be ideal to demonstrate the performance of W-SAFT through the full focal field. For the non-scattering case (phantom A), the unfocused beam output from the fiber was significantly narrower than the FOV of the transducer and thus, with optically dictated lateral resolution, the scan can be considered to be of the OR type. With the inclusion of the intralipid in phantom B, the beam was sufficiently scattered for the scan to be considered to be of the AR type.

In the simulated scan, the surface was modeled and therefore known. In the phantom experiments, the surfaces were positioned close to the transducer and set to be parallel to the scanning x–y plane. This was done by first taking pulse-echo ultrasound b-scans along x for several positions along y and setting the distance from the transducer to the surface of the agar to be constant.

C. Biological Scan

In the third test, the algorithm was applied to data acquired from an *ex vivo* juvenile zebrafish (35 days post-fertilization) mounted in clear agar. This model organism is a common subject in optoacoustic imaging studies [19] and was selected here because of the high degree of scattering across its volume. The HFOAM system was operated in this case in a fast-scanning mode applying no averaging, and used a photonic crystal fiber with a gradient-index (GRIN) lens to deliver a diffraction-limited optical focus at a 6.5 mm distance from the lens. With the operating wavelength of 597 nm, the lateral FWHM of the optical spot has previously been measured as 20 μm [12]. The pulse-echo mode of the system was also employed to facilitate anatomical interpretation of the optoacoustic images. The ultrasound scan was 3 × 12 mm in size, of which a 1.6 × 6.1 mm sub-region was optoacoustically scanned. Both volumes were scanned with a 10 μm lateral pixel size without applying signal averaging; the optoacoustic scan was made with a per-pulse laser energy of around 15 μJ.

The per-pulse energy used here was significantly lower than that used in the phantom scan, and shot averaging was also not employed so as to avoid photodamage of the zebrafish specimen.

A map of the optically scattering surface $S(x, y)$ was determined semiautomatically. This value was then used to look up the depth of the scattering surface for any x–y position of the scanning transducer, and thus the beam waist of the unscattered beam. As per the theory section, the scattered beam waist was iteratively estimated as an embedded Gaussian beam, thus giving an estimate of the fluence distribution inside the imaged fish.

D. Preparation of Results

The simulated and experimental data was also processed with a previous implementation of a weighting-based SAFT algorithm, SIR-SAFT [9], which exclusively uses the SIR of the transducer as a weighting field. However, as this algorithm assumes spatially uniform fluence, the output volume was weighted by a fluence-attenuation compensation function, $\boldsymbol{K}_i$, as

$$\boldsymbol{K}_i = \frac{e^{\alpha(z-\boldsymbol{S}_i)}}{\boldsymbol{U}_i(z)},$$
$$\boldsymbol{V}_K = \boldsymbol{V}_i \boldsymbol{K}_i, \tag{9}$$

where $\boldsymbol{S}_i$ is the depth of the optically scattering surface, $\boldsymbol{U}_i(z)$ is the Gaussian beam spreading along z before normalization, and $\boldsymbol{V}_K$ is the weighted SIR-SAFT output.

To form meaningful images of the OR data, such as in Fig. 4, the volume was first polarity-flipped in z about the acoustic focus, and then only one polarity of the volume used, i.e., set all negative values to zero. This is necessary because the result of the W-SAFT method is still a bipolar ultrasound data set. Although one option here is to take MAPs of the absolute value of the Hilbert transform of the volume, there is no gain to be had. This is because where limited contributions exist, namely in the

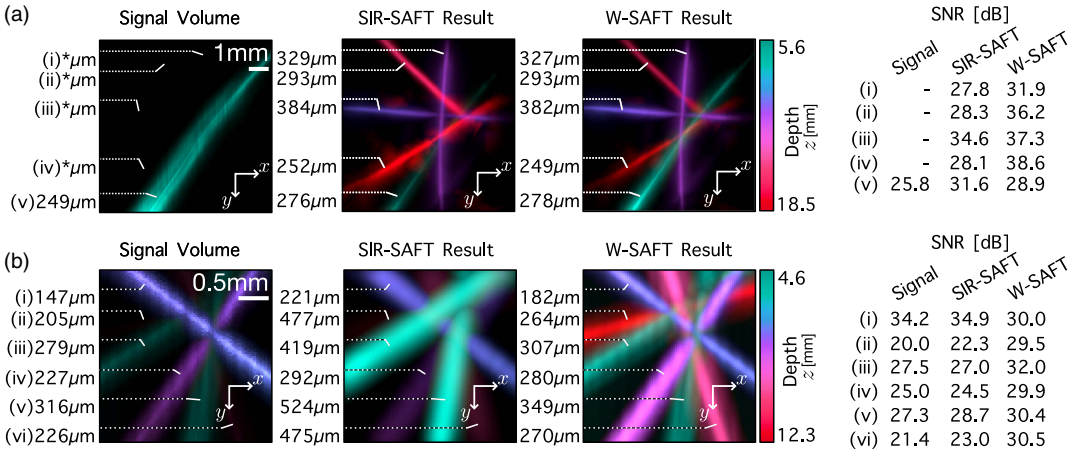

Fig. 4. MAPs for experimental (a) AR data and (b) OR data. In both (a) and (b), the left image is the unprocessed scan volume, and the center and right images are the weighted SIR-SAFT and W-SAFT results, respectively. The MAPs are all in z, with a depth-coded color scale. Each suture is annotated with a label (i)–(v) and a measure of FWHM. The right of each panel shows a table of SNR for each suture.

OR regime, the positive and negative peaks remain temporally discrete and the Hilbert transform of the W-SAFT corrected result has two maxima. Thus, although it would have been possible for the AR case, the one-sided volumes are presented for continuity. The polarity flip about $z' = 0$ is necessary because in these data sets signals from beneath the focus will exhibit a negative-polarity bias, whereas those shallow of the focus exhibit a positive amplitude bias [see, for example, Fig. 3(d)].

Visualization of volumetric signal-dense data presented some additional challenges, especially for the biological scan. Here, MAPs of sub-volumes (thin layers) were chosen as they effectively present sections of 3D structures. It should be noted that in order to improve legibility, histogram-based noise-floor removal was performed for all data presented, i.e., histograms with log-spaced bins were made for all volumes, and a threshold set at the maxima; voxels with an amplitude below the bin value for the maxima were set to 0. This is possible because overwhelmingly more voxels for each volume lie outside the imaged specimen and thus mainly contain noise.

4. RESULTS

A. Numerical Simulations

The results of applying W-SAFT to the simulated data are presented in Fig. 3(iv), demonstrating significant improvement in the out-of-focus lateral resolution in the AR regime ($z' > -0.5$ mm) while retaining optically dictated lateral resolution in the OR regime ($z' < -0.5$ mm). This can be seen both qualitatively from the MAP images in panels (b) and (c), and quantitatively from the full-width half-maximum annotations in (c). The typical individual optoacoustic waveforms in $\boldsymbol{D}$ can be seen in Fig. 3(d). Here, a composite time-domain signal shows how in the OR regime the central signal for a sphere will still have temporally distinct peak amplitudes, even after the W-SAFT processing, due to the limited-contribution effects mentioned previously. Furthermore, with the three major distortion corrections and the fluence-attenuation compensation gain, the difference in normalized amplitude between the highest- and lowest-amplitude peak is 0.56 (iv). This is in contrast to (ii), the results of the weighted SIR-SAFT as per Eq. (9), where the optically resolved data is laterally blurred and the normalized peak–peak amplitude range is 0.98 [see Fig. 3(d)]. The importance of including all the distortion corrections is also clear when comparing the complete W-SAFT algorithm (iv) to the intermediate result (iii) where only the limit function, $\boldsymbol{\Gamma}$ [Eq. (3)], was used.

The signals presented in panel (d) are also composite time-domain signals created from each sphere. After applying W-SAFT, there are still distortions related to the SIR due to insufficient lateral contributions.

B. Phantom Scan

The performance of our method is further confirmed in the experimental results using the agar-suture phantom, as can be seen from Fig. 4. The out-of-focus lateral resolution in AR data [panel (a)] is improved, the lateral resolution in OR data [panel (b)] is maintained below a 19% mean decrease, and in both cases a high degree of peak-to-peak amplitude compression is achieved. In the AR case, the advantages of W-SAFT are even more obvious. In the unprocessed data and the weighted SIR-SAFT result (left and center image), only suture (v) is readily distinguishable due to its proximity to the acoustic focus. Conversely, in the W-SAFT processed data (right image), sutures (i-iv) are also clearly visible both with respect to their lateral resolution and the very small difference in amplitudes. Additionally, W-SAFT can be seen to overall increase the SNR of the scan volumes in both the scattering and non-scattering phantoms.

C. Zebrafish Imaging

Ex vivo juvenile zebrafish imaging results are presented in Fig. 5, including the pulse-echo whole-body scan, original optoacoustic scans, and results of applying the W-SAFT method to the optoacoustic data. Panel (a) shows the B-scan images of the pulse-echo ultrasound data (gray), the mask for the optically scattering surface (color), and three regions through which partial-volume MAPs were made (dashed boxes).

Panel (b) presents said small-volume MAPs (i)–(iii) through (1) signal volume, (2) weighted SIR-SAFT result, (3) W-SAFT result, (4) W-SAFT result with annotations of key anatomical features, and (5) annotated pulse-echo ultrasound signal cross sections.

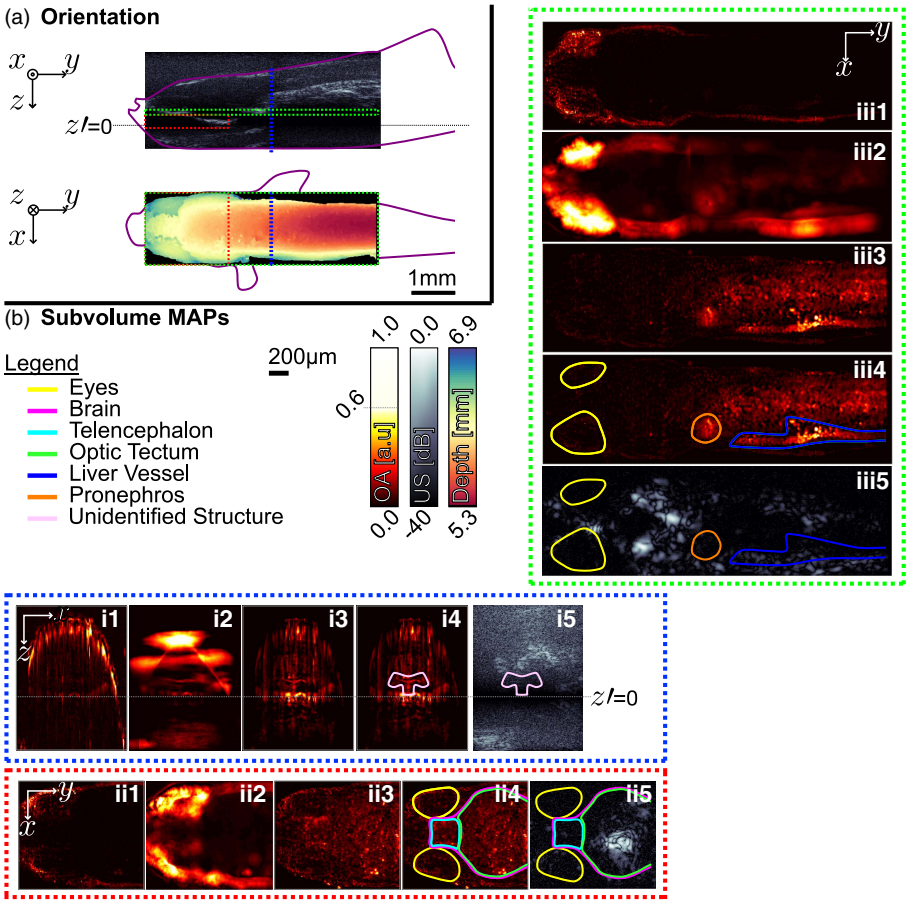

Fig. 5. (a) Top: b-scan of ultrasound data; bottom: surface depth mask. The boundaries of three subvolumes (i)–(iii) are shown as red, green, and blue boxes, respectively. MAPs of these subvolumes were made for the optoacoustic data, and are presented in (b). For each subvolume (i)–(iii), MAPs are shown for (1) signal volume, (2) SIR-SAFT result, (3) W-SAFT result, (4) annotated W-SAFT result, and (5) cross sections through two of three dimensions for SAFT-processed pulse-echo ultrasound data (as labeled); these are also annotated.

It can be clearly seen how W-SAFT affects the image quality. For instance, in all three of the sub-volumes [Figs. 5(b.i)–5(b.iii)], the MAPs for the unprocessed data volumes [Figs. 5(b.ii1) and 5(b.iii1)] are largely shell-like (i.e., only voxels from the periphery of the fish are visible) before the incident beam is scattered and attenuated. In the SIR-SAFT result [Figs. 5(b.i3)–5(b.iii3)], the images are blurred because the impinging fluence is not diffuse. In contrast, in the W-SAFT results [Figs. 5(b), 5(b.ii3), 5(b.ii4), 5(b.iii3), and 5(b.iii4)], the volumes are more complete, namely, the signal amplitudes are more evenly distributed across the entire fish volume. Here the added value of optoacoustic images is also evident, as, although the pulse-echo ultrasound images are very useful in orientation of the target (top), the cross sections in Fig. 5(b) show very few features due to the lack of reflection-based contrast. In the head subvolume [Fig. 5(b.ii)], the W-SAFT result [Fig. 5(b.ii4)] gives a coronal cross section of the eyes and the brain, outlined in yellow and magenta, respectively. The brain section shows the telencephalon (cyan) and the front of the optic tectum (green). Although the eyes are present in the unprocessed data [Fig. 5(b.ii1)], the brain is only visible in the W-SAFT processed volume [Figs. 5(b.ii3) and 5(b.ii4)]. Again, the SIR-SAFT result is not an improvement upon the unprocessed signal volume. In the torso subvolume [Fig. 5(b.i)], the W-SAFT processing further reveals anatomical features located just behind the pronephros and above the anterior swim bladder, which could not be clearly identified from the atlas (peach). This unidentified structure is not easily seen in the signal volume [Fig. 5(b.i1)], whereas it is readily observed in the W-SAFT result [Figs. 5(b.i3) and 5(b.i4)]. Here the shortcomings of SIR-SAFT are clear [Fig. 5(b.i2)], where, due to its lack of consideration for the optical fluence, the surface of the fish is heavily blurred. In the anterior subvolume [Figs. 5(b.iii3) and 5(b.iii4)], the W-SAFT result reveals the upper-left portion of the pronephros (orange) and a major vessel inside the liver (blue). These anatomical features were identified and labeled based on a qualitative comparison of the reconstructed optoacoustic volumes with the optical projection tomography atlas [20].

5. DISCUSSION

The first effort trialed here at retaining optically dominated resolution in HFOAM data was a modification of the previously published SIR-SAFT algorithm [9], where the weighting field employed was updated from the SIR alone to include fluence-based spatial masking as per Eq. (9). Through testing on simulated data [see Fig. 3(d.ii)], this was shown to be a flawed approach, thus illustrating the necessity of W-SAFT.

One observation that must also be made for the AR phantom data [Fig. 4(a)] is that the 50 μm sutures appear to have a FWHM

of around 300 μm in the W-SAFT output. This is because the system is detecting tilted cylindrical waves with a spherical surface, which results in significant low-pass filtering effects that are detrimental to the frequency-dependent lateral resolution of the system. In the OR case in Fig. 4(b), it can be observed that the amplitude correction is of significant advantage as all sutures are visible within a very close amplitude range. With respect to the lateral resolution, it can be observed that W-SAFT has little distorting effect (recall pixel dimension of 30 μm^2). One may still wonder as to why W-SAFT does not improve lateral resolution in the OR regime. This is best explained by observations made in the AR data where it was shown that, given all possible lateral contributions, a suture phantom of this nature was only resolvable to a resolution of around 300 μm. As a result, the limited-contribution case of the OR data cannot be expected to outperform the broad-contribution AR case involving summation over a large number of scanning positions. Indeed, the FWHM measures of the sutures in volume (a) can be seen to, on average, be less than 300 μm. Thus, W-SAFT is performing exactly as desired with respect to its lateral resolution performance.

The brighter posterior region of the fish subvolume in Figs. 5(b.iii3) and 5(b.iii4) is due to the presence of a region of low acoustic impedance, which acts as a partially reflective plane. The presence of this region was confirmed from the pulse-echo ultrasound data presented in Fig. 5(b.iii5). Namely, acoustic waves from optoacoustic sources very close to (or at) this boundary, due to the immediate acoustic mismatch, undergo a more one-sided propagation, e.g., hemispherical rather than spherical. This results in a considerably higher net signal amplitude detected for this region of the fish.

Overall the signal to noise ratio was seen to increase after W-SAFT in the phantom data and the *ex vivo* fish data. This was to be expected because of the constructive and destructive interference that occurs during summation of data containing both real signals and noise, respectively. In addition, the dynamic range compression is seen to give better contrast to noise ratio for the simulated, phantom, and *ex vivo* data.

As mentioned in Section 3.D, where W-SAFT processes signals with limited lateral contributions, the resultant signal will retain temporally discrete positive and negative peaks. Such data is typical of focused transducers operating in the OR regime. This is a physical limitation that is not surpassable, and although W-SAFT may improve the degree to which the peaks are discrete, the frequency-domain distortion present in the original signal will remain intact to some degree.

In this work, the gain function applied is intended to compensate for the fluence losses. However, for further improvements still, acoustic attenuation of the volume should also be considered. This compensation, as per [21], can readily be applied in conjunction with W-SAFT as a pre-processing step for the scan volume. One advantage here would be that the gain function would more reliably compensate for fluence losses rather than the combined effect of fluence loss and acoustic attenuation.

Overall, it is hoped that the development of W-SAFT will allow OAM to significantly develop in the field of small animal imaging. Here, investigations are often limited to either high-resolution superficial scanning or lower-resolution imaging at depths. With W-SAFT, it should be possible to bridge this resolution-penetration gap by scanning simultaneously in both OR and AR regimes. However, the tightly focused light beam used by the particular HFOAM implementation used in the current validation studies may limit the effective penetration *in vivo*, in particular in the AR imaging regime. This is because the maximal imaging depth generally scales with the amount of energy deposited by each excitation laser pulse, which is in turn constrained by the laser fluence safety limits. Yet the latter fluence-penetration trade-off can be potentially improved by devising more advanced illumination approaches specifically tailored for the hybrid OR/AR microscopy. Finally, it should be noted that W-SAFT is in fact a universal methodology generally applicable not only to the particular HFOAM method used in our validation studies but also to a wide palette of scanning-based optoacoustic imaging techniques employing non-uniform and/or varying illumination, such as AR microscopy [3], raster-scan optoacoustic mesoscopy [22], or even tomographic approaches using scanning of focused array transducers [23–25].

6. CONCLUSION

Data acquired from typical scanning OAM systems is strongly affected by both the spatially varying sensitivity field of the detector and highly inhomogeneous light distribution across the imaged volume. Accurate image reconstruction thus implies accounting for both effects, which has been efficiently implemented here by means of the newly developed weighted synthetic aperture focusing technique, the W-SAFT. This lightweight and fast algorithm was showcased to simultaneously retain optical resolution characteristics at superficial tissue depths, and improve the acoustic resolution performance while also compressing peak amplitudes to a tight dynamic range without loss of context. Furthermore, W-SAFT has been shown to work on simulated, phantom, and *ex vivo* biological data, and is the first optoacoustic algorithm to be applied successfully that accounts for moving, highly variant optical fluence. Future work may focus on further improvements through inclusion of a more dexterous scattered-beam model, making use of structural information from ultrasound data.

Funding. H2020 European Research Council (ERC) (ERC-2015-CoG-682379).

REFERENCES

1. V. Ntziachristos, "Going deeper than microscopy: the optical imaging frontier in biology," Nat. Methods **7**, 603–614 (2010).
2. L. V. Wang, "Multiscale photoacoustic microscopy and computed tomography," Nat. Photonics **3**, 503–509 (2009).
3. R. Ma, S. Söntges, S. Shoham, V. Ntziachristos, and D. Razansky, "Fast scanning coaxial optoacoustic microscopy," Biomed. Opt. Express **3**, 1724 (2012).
4. E. M. Strohm, M. J. Moore, and M. C. Kolios, "High resolution ultrasound and photoacoustic imaging of single cells," Photoacoustics **4**, 36–42 (2016).
5. S.-L. Chen, Z. Xie, L. J. Guo, and X. Wang, "A fiber-optic system for dual-modality photoacoustic microscopy and confocal fluorescence microscopy using miniature components," Photoacoustics **1**, 30–35 (2013).
6. K. Maslov, H. F. Zhang, S. Hu, and L. V. Wang, "Optical-resolution photoacoustic microscopy for *in vivo* imaging of single capillaries," Opt. Lett. **33**, 929–931 (2008).
7. R. G. Maev, *Acoustic Microscopy: Fundamentals and Applications* (Wiley, 2008).
8. M.-L. Li, H. F. Zhang, K. Maslov, G. Stoica, and L. V. Wang, "Improved *in vivo* photoacoustic microscopy based on a virtual-detector concept," Opt. Lett. **31**, 474–476 (2006).

9. J. Turner, H. Estrada, M. Kneipp, and D. Razansky, "Improved optoacoustic microscopy through three-dimensional spatial impulse response synthetic aperture focusing technique," Opt. Lett. **39**, 3390–3393 (2014).
10. M. Á. Araque Caballero, A. Rosenthal, J. Gateau, D. Razansky, and V. Ntziachristos, "Model-based optoacoustic imaging using focused detector scanning," Opt. Lett. **37**, 4080–4082 (2012).
11. X. L. Deán-Ben, H. Estrada, M. Kneipp, J. Turner, and D. Razansky, "Three-dimensional modeling of the transducer shape in acoustic resolution optoacoustic microscopy," Proc. SPIE **8943**, 89434V (2014).
12. H. Estrada, J. Turner, M. Kneipp, and D. Razansky, "Real-time optoacoustic brain microscopy with hybrid optical and acoustic resolution," Laser Phys. Lett. **11**, 045601 (2014).
13. R. Cao, J. P. Kilroy, B. Ning, T. Wang, J. A. Hossack, and S. Hu, "Multispectral photoacoustic microscopy based on an optical-acoustic objective," Photoacoustics **3**, 55–59 (2015).
14. A. E. Siegman, "How to (maybe) measure laser beam quality," in *DPSS (Diode Pumped Solid State) Lasers: Applications and Issues* (Optical Society of America, 1998), paper MQ1.
15. F. Träger, *Springer Handbook of Lasers and Optics* (Springer, 2012).
16. A. Rosenthal, D. Razansky, and V. Ntziachristos, "Fast semi-analytical model-based acoustic inversion for quantitative optoacoustic tomography," IEEE Trans. Med. Imaging **29**, 1275–1285 (2010).
17. J. A. Jensen, "Field: A program for simulating ultrasound systems," in *10th Nordic Baltic Conference on Biomedical Imaging* (Citeseer, 1996), Vol. **4**, pp. 351–353.
18. H. Estrada, E. Sobol, O. Baum, and D. Razansky, "Hybrid optoacoustic and ultrasound biomicroscopy monitors' laser-induced tissue modifications and magnetite nanoparticle impregnation," Laser Phys. Lett. **11**, 125601 (2014).
19. M. Kneipp, H. Estrada, A. Lauri, J. Turner, V. Ntziachristos, G. G. Westmeyer, and D. Razansky, "Volumetric tracking of migratory melanophores during zebrafish development by optoacoustic microscopy," Mech. Dev. **138**, 300–304 (2015).
20. D. Salgado, C. Marcelle, P. D. Currie, and R. J. Bryson-Richardson, "The zebrafish anatomy portal: A novel integrated resource to facilitate zebrafish research," Dev. Biol. **372**, 1–4 (2012).
21. B. E. Treeby, "Acoustic attenuation compensation in photoacoustic tomography using time-variant filtering," J. Biomed. Opt. **18**, 036008 (2013).
22. M. Omar, J. Gateau, and V. Ntziachristos, "Raster-scan optoacoustic mesoscopy in the 25–125 Mhz range," Opt. Lett. **38**, 2472–2474 (2013).
23. A. Chekkoury, J. Gateau, W. Driessen, P. Symvoulidis, N. Bézière, A. Feuchtinger, A. Walch, and V. Ntziachristos, "Optical mesoscopy without the scatter: broadband multispectral optoacoustic mesoscopy," Biomed. Opt. Express **6**, 3134–3148 (2015).
24. D. Razansky, M. Distel, C. Vinegoni, R. Ma, N. Perrimon, R. W. Koster, and V. Ntziachristos, "Multispectral opto-acoustic tomography of deep-seated fluorescent proteins *in vivo*," Nat. Photonics **3**, 412–417 (2009).
25. D. Razansky, A. Buehler, and V. Ntziachristos, "Volumetric real-time multispectral optoacoustic tomography of biomarkers," Nat. Protoc. **6**, 1121–1129 (2011).